Effect of 0.40 % and 0.20 % Titanium Addition on Microstructure Properties and Corrosion Behavior of $CuAl_{10}Ni_5Fe_4$ Alloy

Abubaker J. A. IRHAYIM [1], Ismail ESEN [1] *, Selami SAGIROGLU [1], Esma KESKIN [2], Hayrettin AHLATCI [3], Volkan KARAKURT [4]

[1] *Mechanical Engineering, Faculty of Engineering, Karabuk University, Karabuk 78050, Turkey*
[2] *BUMA Engineering and Consulting Inc., Ankara, 6980, Turkey*
[3] *Metallurgical and Materials Engineering, Faculty of Engineering, Karabuk University, Karabuk 78050, Turkey*
[4] *Sağlam Metal San. Tic. A.Ş, Kocaeli, Turkey*

http://doi.org/10.5755/j02.ms.41403

Received 5 May 2025; accepted 30 May 2025

This study examined how post-casting heat treatment (solution treatment and tempering) and forging affected the corrosion and microstructural properties of the nickel aluminium bronze ($CuAl_{10}Ni_5Fe_4$) with 0.20 % and 0.40% titanium addition. Heat-treated $CuAl_{10}Ni_5Fe_4$ alloy microstructures showed copper-rich α-solid solution, martensitic β-phase, and intermetallic κ-phases, such as flake-shaped κI, fine κIII, and black globular κIV. Adding 0.20 % and 0.40 % titanium to $CuAl_{10}Ni_5Fe_4$ alloys reduced dendritic arm thickness and increased κ phase abundance. Additionally, significant κIV and κII precipitations were observed in the tempered β phase. Tempering β may cause martensitic β to split into tiny α and κIII phases. The grain refinement of the $CuAl_{10}Ni_5Fe_4$, $CuAl_{10}Ni_5Fe_4$-0.20 % Ti, and $CuAl_{10}Ni_5Fe_4$-0.40 % Ti alloys was significantly noticeable after forging. The alloys retained the same α, β, and κ phases seen in the heat-treated alloys after forging. Titanium's refining effect increased the hardness of the alloy into which it was incorporated. Increased stiff phases, such as tempered β and fine κIV, contribute to increased hardness. The forging process enhanced the hardness of all three alloys. Forged and heat treated $CuAl_{10}Ni_5Fe_4$-0.40 % Ti alloy had the highest hardness with 243.50 HB and 256.18 HB, respectively. The microstructural phases α, β, and κ significantly impact the corrosion behaviour of $CuAl_{10}Ni_5Fe_4$ alloy. The $CuAl_{10}Ni_5Fe_4$-0.40 % Ti alloy after forging had the lowest 24-hour weight loss of 0.003326 mg/dm^2. The $CuAl_{10}Ni_5Fe_4$ alloy loses the most weight (0.013659 mg/dm^2) following heat treatment (S.T.+T) after 24 hours. The minimal corrosion rate for the $CuAl_{10}Ni_5Fe_4$-0.40 % Ti alloy after forging was 0.003916 mg/(dm^2·day) after 72 hours. Due to stratification, corrosion creates craters. Pitted or porous structures and craters are common. All alloys show a decrease in these structures after forging. The formation of the $CuCl_2$ phase is believed to occur in regions experiencing pitting corrosion.

Keywords: $CuAl_{10}Ni_5Fe_4$, heat treatment, forging process, corrosion behavior, microstructure.

1. INTRODUCTION

Bronze alloys have been a significant material in various industrial applications due to their exceptional properties such as corrosion resistance, mechanical strength, and durability. Nickel aluminum bronze (NAB) and manganese aluminum bronze (MAB) are two highly alloyed bronzes that have gained popularity for their resistance against corrosion, cavitation, erosion, and improved mechanical properties [1]. These alloys are extensively used in marine applications like marine propellers due to their high strength and excellent corrosion resistance [2]. The addition of nickel to aluminum bronze has been explored to enhance properties like corrosion resistance, hardness, tensile strength, and wear resistance [3]. Historically, bronze was the first intentionally man-made alloy, typically composed of copper and tin in varying proportions [4]. The transition from arsenical copper alloys to tin alloys marked the Bronze Age, where bronze became the predominant alloy [5]. The production of bronze involved smelting copper and tin ores to create the desired alloy [6–8]. Different regions and time periods exhibited variations in bronze compositions, with some containing additional elements like lead [9, 10].

Bronze alloys have also been studied for their microstructural characteristics and processing techniques. Research has focused on enhancing properties through processes like friction stir processing and post-heat treatments [11, 12]. Studies have shown that copper-based alloys, including bronze, offer superior corrosion resistance for maritime applications [13]. Furthermore, the use of high-alloy bronzes like NAB and MAB has been highlighted for specific applications, showcasing their appropriateness and effectiveness [14]. Nickel aluminum bronze (NAB) is a copper-based alloy that typically contains aluminum, nickel, iron, and manganese elements [15]. The microstructure of NAB is crucial for its properties, including corrosion resistance, cavitation resistance, and mechanical strength [16]. The alloy's microstructure usually consists of α phase, β phase, and κ phase [15]. Studies have shown that the addition of elements like cobalt and titanium can influence the properties of NAB, affecting its corrosion and wear resistance [17]. Furthermore, the microstructure of NAB can

* Corresponding author: I. Esen
E-mail: *iesen@karabuk.edu.tr*

be modified through processes like friction stir processing, leading to the transformation of the initial coarse microstructure into a finer structure with improved properties [18]. The corrosion resistance of NAB is a significant aspect, especially in marine applications. The alloy's resistance to corrosion is attributed to the formation of a protective oxide film on its surface [19 – 21]. The development of protective surface layers and corrosion product films on NAB alloys has been identified as a critical factor in enhancing their corrosion resistance [19, 22]. Heat treatment has been found to impact the microstructure evolution and erosion-corrosion behavior of NAB in chloride solutions [23]. Additionally, the morphology, crystallography, and chemistry of phases in as-cast NAB play a crucial role in determining its properties [24].

The phase transition that takes place during heat treatment is the main factor that controls the microstructure of NAB alloys. When the temperature exceeds 1030 °C, the NAB exhibits the β phase. As the temperature decreases, the α phase begins to develop within the β phase. At a temperature of 930 °C, the κII phase begins to separate from the β phase. At a temperature of 860 °C, the κIV phase forms as a result of precipitation from the α phase. The formation of the eutectoid α + κIII phase occurs when the residual β phase is cooled below 800ºC. Aside from temperature, the pace at which something cools down is also crucial in determining the phase change and the ensuing composition of phases. If the cooling rate is not slow enough, the β phase may persist as the β′ phase with a martensitic microstructure, leading to a detrimental impact on the corrosion resistance of the alloy. Therefore, the NAB is often subjected to annealing at a temperature of 675 °C in order to remove the remaining β phase [25 – 27]. Prior research has been conducted to examine the impact of heat treatment and hot working on the microstructure and mechanical characteristics of NAB alloys [28, 29]. Currently, there has been a scarcity of research conducted on the impact of heat treatment on the erosion-corrosion resistance of NAB alloys. Furthermore, the correlation between the microstructure of the NAB and its erosion-corrosion behavior has yet to be determined.

Titanium addition to nickel aluminum bronze alloys has been a subject of interest in various studies. investigated the impact of adding titanium as a grain refiner along with cobalt to nickel-containing aluminum bronze [17]. The study focused on properties in both cast and forged conditions. Incorporating titanium into nickel aluminum bronze alloys has shown potential for enhancing properties such as corrosion and wear resistance. Titanium, when utilized as a grain refiner, impacts the microstructure of NAB, consequently affecting its corrosion resistance [16]. Additionally, the design of the microstructure to enhance the corrosion and cavitation resistance of NAB often considers the inclusion of titanium [16]. Furthermore, the addition of titanium to nickel aluminum (Raney) alloys used for hydrogen electrodes in alkaline hydrogen-oxygen fuel cells has been investigated, indicating that titanium may play a role in improving the corrosion resistance of nickel aluminum alloys [30]. Moreover, the literature indicates that nickel aluminum bronze alloys are widely used in various applications, including ship propellers [15]. This underscores the importance of understanding how different alloying elements, such as titanium, can influence the mechanical properties and corrosion resistance of these alloys.

Finally, the microstructure of nickel aluminium bronze plays an important role in defining its mechanical, corrosion, and cavitation resistance qualities. Several studies have investigated the impacts of various elements, heat treatments, and processing methods on the microstructure of NAB, highlighting the importance of microstructural design in improving the alloy's performance. The ability to improve properties including corrosion resistance, wear behaviour, and heat treatment techniques by adding up to 0.4 % titanium to nickel aluminium bronze alloys is investigated here, and the importance of alloy composition in adapting to industrial applications is demonstrated. This study examined the effects of post-casting heat treatment (solution treatment and tempering) and forging techniques on the corrosion and microstructural characteristics of nickel aluminium bronze ($CuAl_{10}Ni_5Fe_4$) that had 0.20 % and 0.40 % Ti added.

2. MATERIALS AND METHODS

The casting studies for the fabrication of samples were conducted at the R&D Center of Saglam Metal Industry and Trade. A pre-prepared nickel aluminum bronze ingot was obtained specifically for use as a raw material in casting experiments, following the manufacturing parameters. Ingots manufactured in industrial settings were utilized as the primary material, whereas materials intended for laboratory research were generated. The ingot, which served as the raw material for casting experiments, was manufactured using the permanent mold casting process and consisted of pure copper scrap, pure aluminum, iron, and nickel. The melting process was conducted using an induction furnace with a capacity of 300 kg. The pre-produced nickel aluminum bronze ingot was sliced and utilized for the melting process. The CuLi prealloy was employed to eliminate oxygen from the liquid metal, while a 30 % copper titanium prealloy was utilized to introduce titanium. The degassing procedure after melting nickel aluminum bronze involved the use of copper lithium prealloy. Three distinct charges were formulated, with one devoid of titanium, another having 0.20 % Ti, and the last one containing 0.40 % Ti. Additionally, 30 % copper titanium prealloy was introduced to the molten metal during the last phase of melting, after which the casting process commenced. The castings were conducted at a temperature of 1230 °C. Table 1 presents the chemical composition of $CuAl_{10}Ni_5Fe_4$, $CuAl_{10}Ni_5Fe_4$-0.20 % Ti and $CuAl_{10}Ni_5Fe_4$-0.40% Ti alloys. The chemical analysis of the ingot produced under industrial conditions was determined using an Oxford brand optical emission spectrometer at the facilities where the casting was carried out. The phases of the alloy were determined using X-ray diffractometry (XRD Rigaku Ultima IV; Japan) with a scanning range of 10 – 90° and a scanning speed of 3°/min. Heat treatments were applied to the samples produced by the casting method, after solution treatment at 875 °C for 90 minutes and then tempering at 650 °C for 2 hours.

Table 1. Weight percentages of alloy compositions

	Chemical composition, wt.%				
Alloy	Al	Fe	Ni	Ti	Cu
$CuAl_{10}Ni_5Fe_4$	10.19	3.01	4.41	–	Bal.
$CuAl_{10}Ni_5Fe_4$-0.20 % Ti	9.99	3.00	4.30	0.2	Bal.
$CuAl_{10}Ni_5Fe_4$-0.40 % Ti	9.87	2.99	4.27	0.4	Bal.

Industrial circumstances were employed to conduct forging (F.) investigations utilizing a ram. The forging conditions were established at a temperature of 870 °C [29], which is known to yield the maximum strength values according to the literature, and a deformation rate of 80 % [31]. In order to achieve this objective, cylindrical metal bars of 68 mm in diameter were subjected to a forging process, resulting in a final section size of 27 × 27 mm, using a ram as a tool.

The $CuAl_{10}Ni_5Fe_4$, $CuAl_{10}Ni_5Fe_4$-0.20 % Ti and $CuAl_{10}Ni_5Fe_4$-0.40 % Ti samples, which had undergone heat treatment and forging, were each cut into dimensions of 10 × 20 × 10 mm. The cutting operation was carried out using a water-cooled band saw. Once the cutting procedure was finished, the samples underwent sanding and polishing using the Mikrotest brand automated apparatus. Various grit grits, including 320, 400, 600, 800, 1000, and 2500, were used throughout the sanding operation. After the sanding operation, the polishing was carried out using a 3 μm Al_20_3 liquid solution. The etching method utilized 5 grams of $FeCl_3$, 50 milliliters of HCl, and 100 milliliters of clean water. A LOM-Carl Zeiss light optical microscope was employed to observe the alterations in the grains inside the phase structure. Additionally, SEM-Carl Zeiss Ultra Plus scanning electron microscope and EDX (energy dispersive X-ray spectroscopy) were utilized to analyze and uncover any secondary phases. Steel balls with a diameter of 2.5 mm were subjected to a force of 187.5 N in order to measure their Brinell hardness.

The immersion corrosion experiment utilized cylindrical samples measuring 10 × 10 × 10 in size. Each sample was subjected to surface area and weight measurements using a Precisa precision balance. The duration of immersion corrosion in a 3.5 % NaCl solution ranged from 12 to 72 hours. Chromic acid and ethanol, derived from 180 grams of CrO_3 and 1 liter of distilled water, were employed to eliminate corrosion residues from the sample surface on an hourly basis. The corrosion samples were first submerged in chromic acid for approximately 3 minutes, then washed with purified water to eliminate any remaining acid residue. The corrosion samples underwent a rinsing process using distilled water, followed by immersion in ethanol for a duration of about 2 minutes, and subsequently were dried. After the drying process, each corrosion sample was carefully weighed using precise scales and then exposed to immersion corrosion once again. The weight losses reported at each hour interval were converted from grams to milligrams as a result of the immersion corrosion process. The surface area of the corrosion sample was converted from mm^2 to dm^2. The milligram lost per square decimeter per hour was determined by dividing the average weight loss (mg) by the surface area (dm^2). The weight reductions were determined by subtracting the beginning value from the end amount. The weight loss after 24 h was determined by subtracting the initial weight/surface area measurement from the weight/surface area measurement taken after 24 h. The corrosion rate was measured in milligrams per square decimeter per day ($mg/dm^2 \times day$). The corrosion rates per day were determined by dividing the weight losses by the duration in days. To determine the corrosion rate corresponding to a 3-day period, the weight loss after 72 h is divided by 3.

3. RESULTS AND DISCUSSION

3.1. XRD patterns

X-ray diffraction (XRD) is a powerful technique used to analyze the crystal structure of materials. In the case of the $CuAl_{10}Ni_5Fe_4$ alloy, the presence of κ phases has been noted to enhance its mechanical strength without compromising ductility [32]. This indicates that the alloy's mechanical properties are influenced by specific phases within its structure. To further understand the crystallographic characteristics of the $CuAl_{10}Ni_5Fe_4$ alloy, XRD analysis has been employed to identify the different phases present and their distribution within the material. In the XRD analyses given in Fig. 1, copper-rich $AlCu_4$ and α-Cu phases were present in the highest peak, while the α-Cu phase was seen in the final peaks of all alloys. When the peaks of the $CuAl_{10}Ni_5Fe_4$ alloy are examined in Fig. 1 a, it is seen that it starts with AlNi and $AlFe_3$ phases at 30.95°. In Fig. 1 b, in the $CuAl_{10}Ni_5Fe_4$-0.20%Ti alloy, the AlTi phase was seen at 21.90° with the presence of titanium, and immediately afterwards the $AlFe_3$ phase was seen at 27.25°. In the $CuAl_{10}Ni_5Fe_4$-0.40%Ti alloy in Fig. 1 c, the AlTi phase was first seen at 20.80°, and then the $AlCu_4$ phase together with the $AlFe_3$ phase was seen at 27.50°.

3.2. Microstructure

Fig. 2 shows the LOM images of $CuAl_{10}Ni_5Fe_4$, $CuAl_{10}Ni_5Fe_4$-0.20 % Ti and $CuAl_{10}Ni_5Fe_4$-0.40 % Ti alloys after solution treatment and tempering after casting, while Fig. 3 shows the LOM images of these alloys after forging. One of the factors that leads to grain refining with the addition of elements is the rise in the rate at which individual grains form before there is an increase in the number of grain nuclei. The formation of smaller grains occurs when the number of nucleation sites per unit volume rises [33]. The inclusion of titanium is believed to have a grain refining impact by increasing the number of nucleation sites, resulting in the creation of smaller grains. The microstructure shown in Fig. 3 a of the heat-treated $CuAl_{10}Ni_5Fe_4$ alloy is a common representation found in several research on nickel-bearing aluminium bronze. The depiction in Fig. 4 helps clarify the presence of a copper-

rich α-solid solution phase, a martensitic β-phase, and various intermetallic κ-phases, including leaf-shaped κI, thin κIII and black globular κIV [34 – 36].

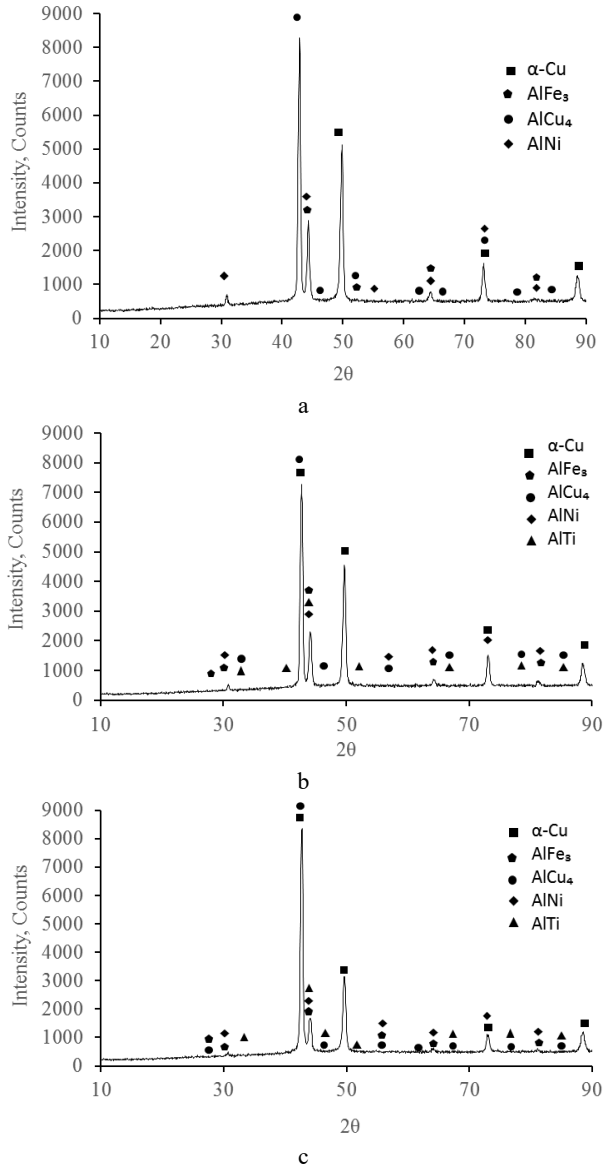

Fig. 1. X-ray diffraction patterns: a – $CuAl_{10}Ni_5Fe_4$, b – $CuAl_{10}Ni_5Fe_4$-0.20 % Ti; c – $CuAl_{10}Ni_5Fe_4$-0.40 % Ti

The depiction in Fig. 4 helps clarify the presence of a copper-rich α-solid solution phase, a martensitic β-phase, and various intermetallic κ-phases, including leaf-shaped κI, thin κIII and black globular κIV [34 – 36].

Fig. 2 b and c show that the addition of 0.20 % and 0.40 % titanium to $CuAl_{10}Ni_5Fe_4$ alloys leads to a decrease in the dendritic arm thickness and an increase in the amount of certain types of κ phases. Additionally, a substantial amount of κIV and κII phase precipitation was observed within the tempered B phase. The tempering of β is believed to cause the martensitic β to decompose into extremely small masses of α and κIII [34].

The decomposition of the martensitic β phase into α and κIII phases during the tempering of the $CuAl_{10}Ni_5Fe_4$ alloy entails the reconstitution of martensite to the high-temperature bcc β phase, which subsequently decomposes into NiAl and α. In Cu-Al-Ni alloys, tempering at 675 °C results in the reconstitution of martensite into the high-temperature β phase, which subsequently decomposes into NiAl and α phases [24].

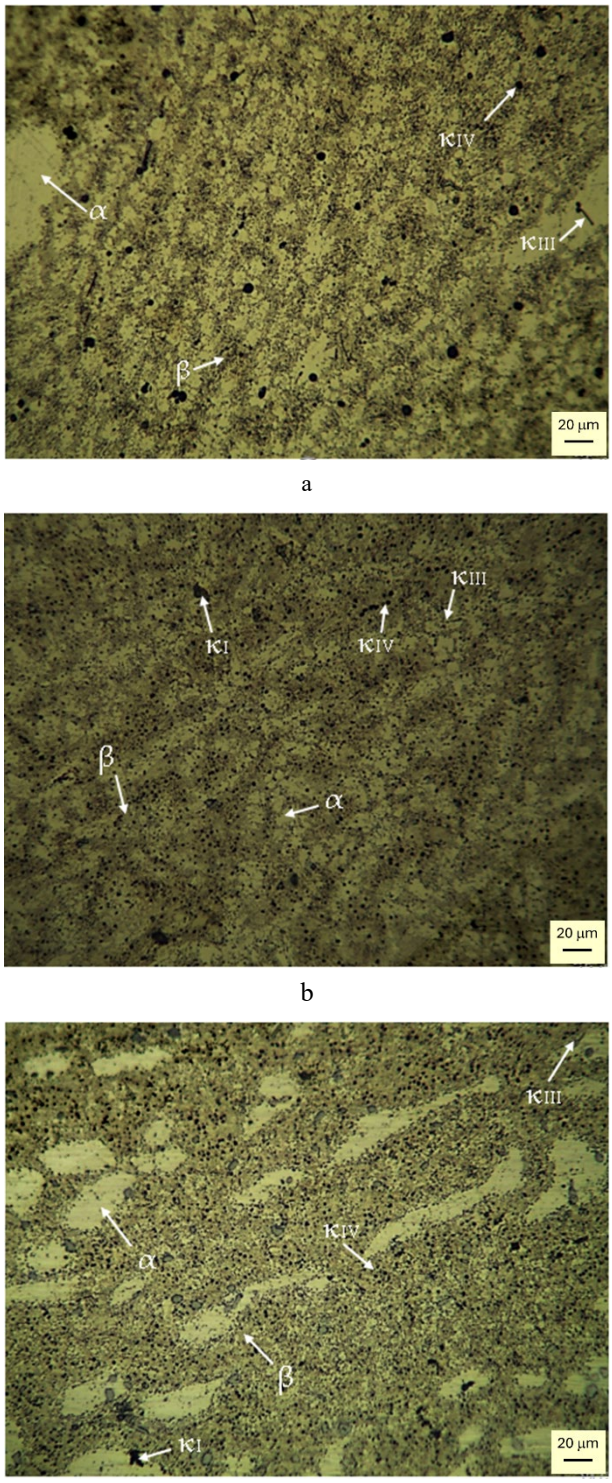

Fig. 2. LOM images after solution treatment and tempering after casting: a – $CuAl_{10}Ni_5Fe_4$; b – $CuAl_{10}Ni_5Fe_4$-0.20 % Ti; c – $CuAl_{10}Ni_5Fe_4$-0.40 % Ti

The procedure encompasses pro-eutectoid γ1 precipitation and eutectoid disintegration, succeeded by dissolution at elevated temperatures [37, 38]. Below 300 °C, a demixing event produces tiny coherent

precipitates, resulting in elevated transition temperatures without altering hysteresis [39].

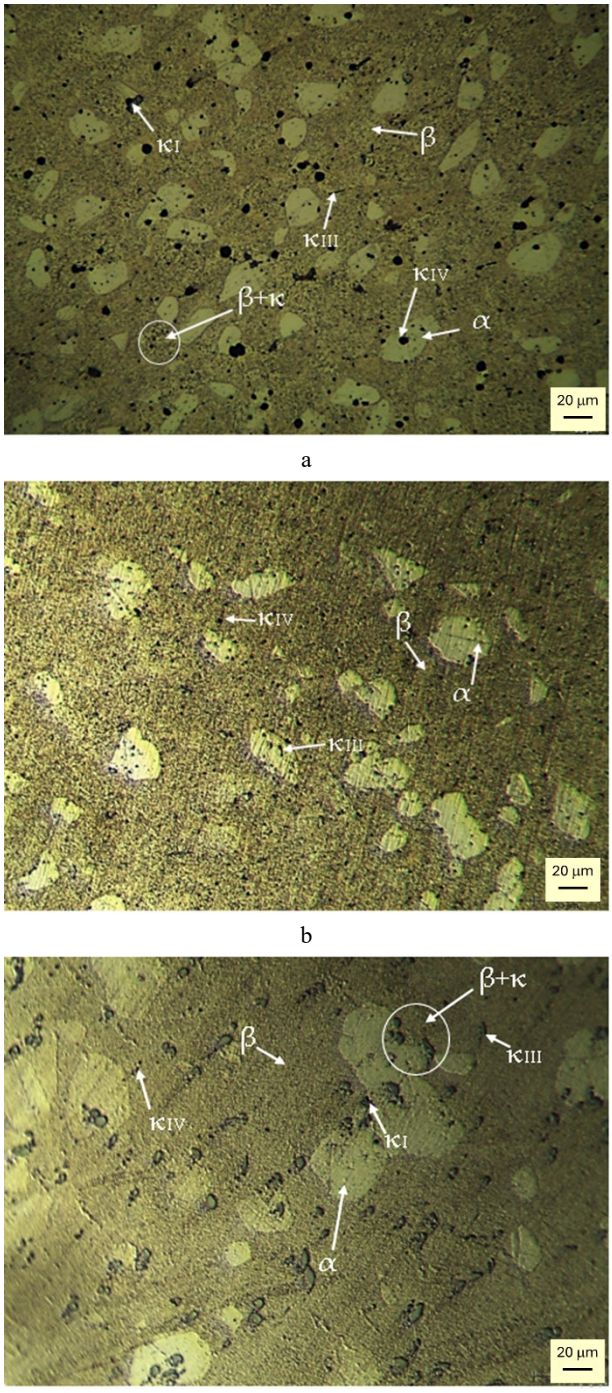

Fig. 3. LOM images after forging: a – $CuAl_{10}Ni_5Fe_4$; b – $CuAl_{10}Ni_5Fe_4$-0.20 % Ti; c – $CuAl_{10}Ni_5Fe_4$-0.40 % Ti

The breakdown process is influenced by elements like elastic stresses from quenching and the level of ordering in the alloy structure [38]. The microstructures of $CuAl_{10}Ni_5Fe_4$, $CuAl_{10}Ni_5Fe_4$-0.20 % Ti and $CuAl_{10}Ni_5Fe_4$-0.40 % Ti alloys were noticeably reduced in thickness after the forging process (Fig. 3). The alloys retained the identical α, β, and κ phases observed in Fig. 2 after the forging process. As a result of the forging process, the dendritic arms were fractured and transformed into almost spherical shapes. Additionally, the forging caused the formation of new κIV phases.

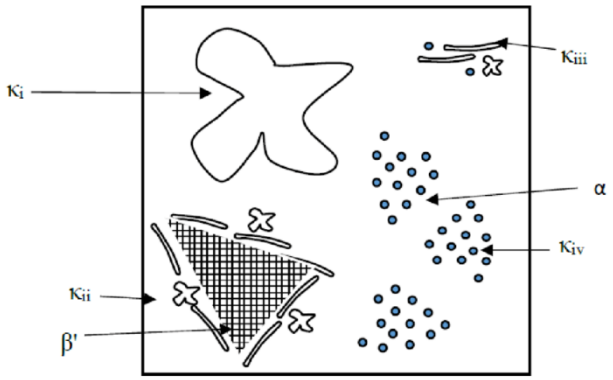

Fig. 4. Illustrations depicting the several stages of a type 80-10-5-5 cast aluminum bronze [34, 35]

The alloys with 0.20 % and 0.40 % titanium addition to the $CuAl_{10}Ni_5Fe_4$ alloy exhibited separate κI and κIII phases. Titanium serves as an inoculant, efficiently enhancing the alloy's microstructure by facilitating the development of finer dendrites. This effect has been shown in many investigations on copper alloys, demonstrating that the incorporation of titanium results in a refined microstructure marked by reduced secondary dendrite arm spacing and therefore finer dendritic characteristics [32]. This refining enhances the alloy's mechanical characteristics, since smaller dendrites often increase tensile strength and ductility. Furthermore, titanium's impact on the production and distribution of κ phases within the $CuAl_{10}Ni_5Fe_4$ alloy structure is essential. The κ phases enhance the mechanical integrity and wear resistance of the alloy, with their production being sensitive to the titanium content. Research findings demonstrate that titanium additions can promote the nucleation of diverse κ intermetallic phases, which display unique morphologies and distributions within the α-Cu matrix [18]. Increased titanium concentration correlates with a higher occurrence of globular κ phase forms, which can boost toughness and mechanical qualities under stress by redistributing stress throughout the alloy [40].

Fig. 5 shows the SEM images of $CuAl_{10}Ni_5Fe_4$, $CuAl_{10}Ni_5Fe_4$-0.20 % Ti and $CuAl_{10}Ni_5Fe_4$-0.40 % Ti alloys after solution treatment and tempering after casting, while Fig. 6 shows the SEM images of these alloys after forging. Table 2 and Table 3 show the EDX analysis of the second phase with distinct morphologies labeled as (1-12) in Fig. 5 and Fig. 6, respectively. The overall SEM images show the microstructure of the alloys consisting of α, β and a series of intermetallic κ phases. The α phase is a copper-enriched solid solution, and the β phase (or retained β phase) is a solid solution with a tempered structure and a high-density AlNi precipitate area. There are three types of κ phases, which are distinguished by the combination of their morphologies and distributions. The κI phase is enriched in iron and is found in the α phase matrix, which typically has a rosette-shaped morphology. The κIV phase is mainly distributed at the α and β boundaries in a spherical-like shape. The κIV phase is much finer than the κI phase.

a

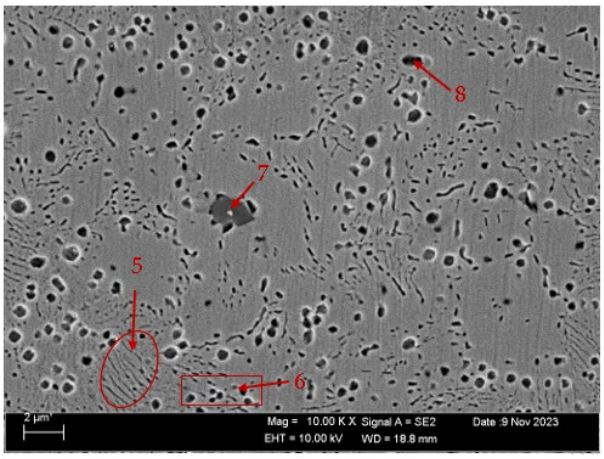

b

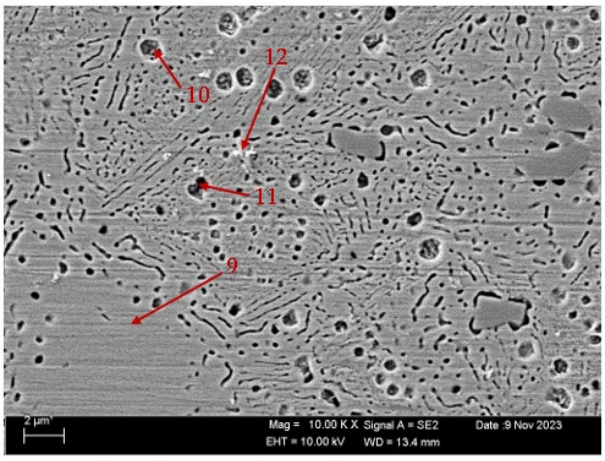

c

Fig. 5. SEM images after solution treatment and tempering after casting: a – $CuAl_{10}Ni_5Fe_4$; b – $CuAl_{10}Ni_5Fe_4$-0.20 % Ti; c – $CuAl_{10}Ni_5Fe_4$-0.40 % Ti

The lamellar κIII phase, which is rich in nickel and forms at the α and β boundaries, is the product of the eutectoid transformation of the β phase at low temperatures. The κIV phase, which is rich in iron, is a finer precipitate within the α phase [21, 41, 42]. The initial cast microstructure of the $CuAl_{10}Ni_5Fe_4$ alloy consists of a combination of several phases, including a copper-rich α solid solution, a β solid solution, and many intermetallic κ phases [32].

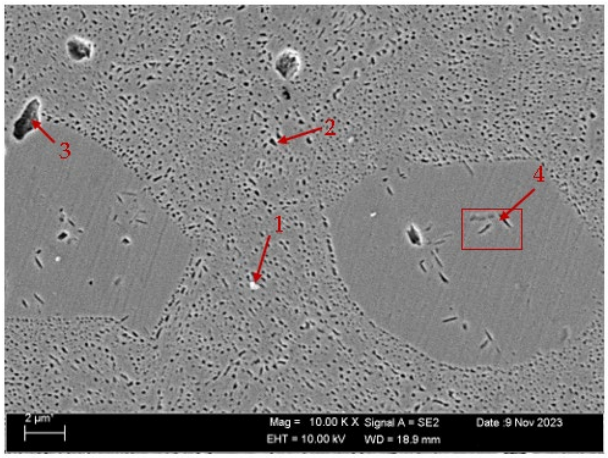

a

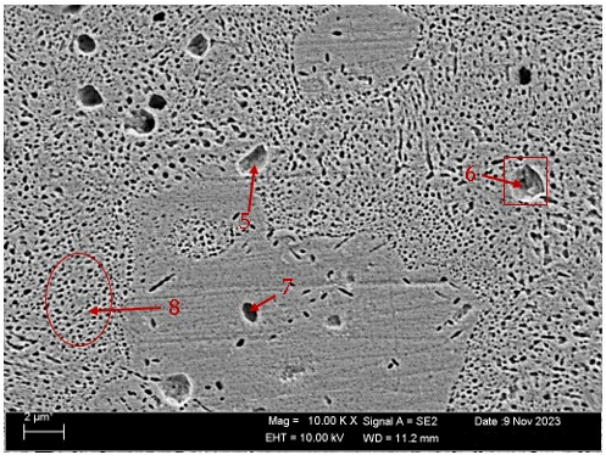

b

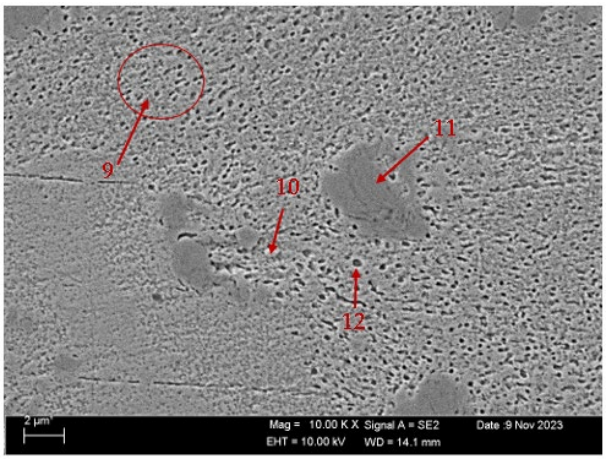

c

Fig. 6. SEM images after forging: a – $CuAl_{10}Ni_5Fe_4$; b – $CuAl_{10}Ni_5Fe_4$-0.20 % Ti; c – $CuAl_{10}Ni_5Fe_4$-0.40 % Ti

The forging process utilises heat and mechanical energy to alter the solid-state structures of the alloy. The κ-phase distribution may be greatly modified; during forging, the stability of several phases, including the κIV phase, is crucially influenced by the temperatures and strain rates applied. The temperature conditions encountered during hot forging frequently enhance diffusion and enable phase changes that may stabilise or result in the emergence of new κ phases.

Table 2. The weight percentage findings of Fig. 5 as determined by EDX

Points	Al	Ti	Mn	Fe	Ni	Cu
1	6.15	–	0.90	–	5.54	87.42
2	1.45	–	1.07	81.11	2.50	13.89
3	6.13	–	1.16	1.19	4.54	86.97
4	4.47	–	1.23	1.25	4.99	88.07
5	6.93	0.06	1.16	–	4.55	87.30
6	7.79	0.11	0.65	–	5.81	85.63
7	1.32	0.08	0.45	2.67	1.40	94.09
8	6.77	0.02	0.75	0.37	6.22	85.88
9	3.51	18.17	0.33	36.96	6.07	34.96
10	4.66	0.23	–	–	4.82	90.29
11	2.21	0.32	2.39	9.55	9.20	76.34
12	16.53	0.36	–	–	4.89	78.21

Table 3. The weight percentage findings of Fig. 6 as determined by EDX

Points	Al	Ti	Mn	Fe	Ni	Cu
1	8.27	–	0.10	0.81	5.60	85.22
2	7.30	–	0.03	0.72	5.01	86.95
3	4.37	–	–	0.32	5.41	89.91
4	6.65	–	0.43	0.22	5.77	86.93
5	6.21	0.06	0.30	1.57	5.55	86.34
6	5.71	0.16	0.24	1.27	5.62	87.00
7	2.81	0.11	1.36	3.87	4.53	87.26
8	6.44	0.14	0.25	0.98	6.31	85.88
9	7.37	0.10	0.41	0.19	6.11	85.85
10	7.70	0.36	1.66	7.12	6.69	76.47
11	2.00	28.09	–	11.38	6.01	52.52
12	10.12	0.38	0.50	6.68	14.13	68.19

Furthermore, the elevated temperature conditions during the forging process might provoke alterations in the pre-existing intermetallic phases. Studies indicate that the emergence of new κ phases, especially κIV, is frequently promoted under dynamic recrystallisation circumstances when the solid solution experiences significant mechanical strain.

Furthermore, the fragmentation and dispersion of coarse particles within the microstructure during the forging process enhance the uniformity of stress distribution. The dynamic recrystallisation process enabled by forging improves the mixing and distribution of alloying elements, hence boosting the overall stability of the κIV phase. The rise in dislocation density and strain can facilitate the formation of nucleation sites for these new phases. The use of elements like as chromium and beryllium facilitates the development of κ phases, notably κIV, during hot forging [43]. Hot forging modifies the microstructure relative to the as-cast state, with torsion experiments replicating the forging process at different temperatures and strain rates [44]. Thermal-mechanical activities, including hot rolling and quenching, impact the development of martensite phases, hence influencing the shape memory effect and the overall characteristics of the alloy [45]. These mechanisms facilitate the formation of several κ phases in conjunction with an α matrix and other intermetallic phases, influencing the alloy's mechanical and corrosion characteristics [43].

3.3. Hardness test results

Fig. 7 shows the hardness of $CuAl_{10}Ni_5Fe_4$, $CuAl_{10}Ni_5Fe_4$-0.20 % Ti and $CuAl_{10}Ni_5Fe_4$-0.40 % Ti alloys after solution treatment and tempering after casting and after forging in a comparative manner. The purpose of the comparison is to analyze the differences in hardness between the different alloys and processing methods. The hardness values of the $CuAl_{10}Ni_5Fe_4$ alloy were found to be lower in comparison to other alloys, when titanium was not added. Grain refining plays a crucial role in improving the hardness characteristics of alloys.

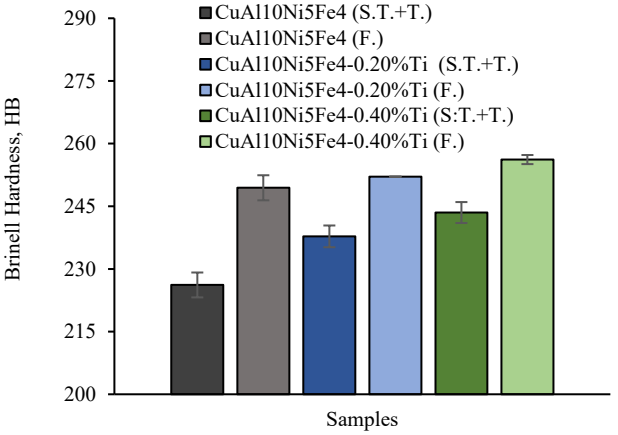

Fig. 7. Comparative hardness results of $CuAl_{10}Ni_5Fe_4$, $CuAl_{10}Ni_5Fe_4$-0.20 % Ti and $CuAl_{10}Ni_5Fe_4$-0.40 % Ti alloys. S.T. – solution treatment; T. – tempering; F. – forging

The enhanced hardness is ascribed to the grain refining phenomenon caused by titanium, resulting in a decrease in grain size and an augmentation in dislocation density [46, 47]. In addition, the inclusion of solid particles in the

alloy as a result of the introduction of grain refiners such as titanium helps to increase the material's hardness [48]. Furthermore, the augmentation in the quantity of rigid phases, namely tempered β and fine κIV, is believed to be another contributing factor to the rise in hardness. Although the process of forging greatly enhanced the hardness of all three alloys, it was observed that the hardness values of $CuAl_{10}Ni_5Fe_4$-0.20 % Ti and $CuAl_{10}Ni_5Fe_4$-0.40 % Ti alloys were similar to each other, however greater than that of the $CuAl_{10}Ni_5Fe_4$ alloy. Considering the difference in hardness values after solution treatment and tempering after casting and after forging, it was observed that $CuAl_{10}Ni_5Fe_4$-0.40 % Ti alloy showed the highest value with 243.50 HB and 256.18 HB values, respectively.

The hardness of the $CuAl_{10}Ni_5Fe_4$ alloy is affected by the α, β, and κ phases, which are determined by the composition and processing conditions. Nickel and iron enhance the stability of the β phase, whereas unidirectional solidification fosters a greater proportion of the α phase relative to gradual cooling [49]. Thermal parameters during solidification influence microstructure, hardness, and microhardness, with elevated aluminium content resulting in enhanced hardness and a more refined structure [50]. Ageing may reduce hardness owing to the production of precipitates and influence grain size in CuAlNi alloys [51].

3.4. Immersion corrosion test results

Fig. 8 shows the comparative 24-hour weight loss changes of $CuAl_{10}Ni_5Fe_4$, $CuAl_{10}Ni_5Fe_4$-0.20 % Ti and $CuAl_{10}Ni_5Fe_4$-0.40 % Ti alloys after solution treatment + tempering and after forging processes. The corrosion rates of these alloys after 72 hours are also given in Fig. 9.

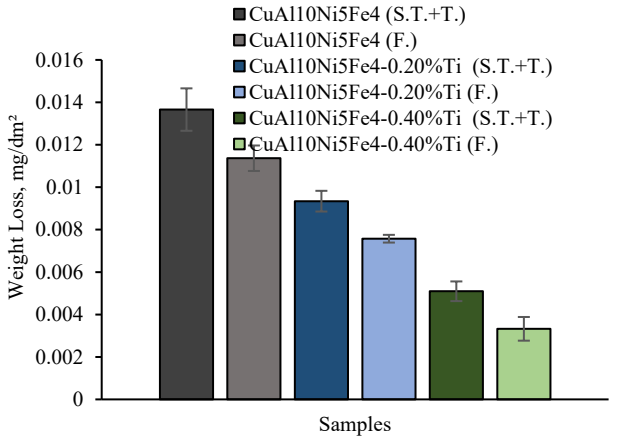

Fig. 8. Comparative immersion corrosion weight loss results of $CuAl_{10}Ni_5Fe_4$, $CuAl_{10}Ni_5Fe_4$-0.20 % Ti and $CuAl_{10}Ni_5Fe_4$-0.40 % Ti alloys. S.T. – solution treatment; T. – tempering; F. – forging

The alloy with 0.40 % Ti addition exhibited the best corrosion behavior after solution treatment + tempering and after forging processes. While the minimum weight loss after 24 hours was found to be 0.003326 mg/dm^2 in the $CuAl_{10}Ni_5Fe_4$-0.40 % Ti alloy after forging process. The maximum weight loss in $CuAl_{10}Ni_5Fe_4$ alloy after solution treatment + tempering was found to be 0.013659 mg/dm^2 after 24 hours. The minimum corrosion rate in $CuAl_{10}Ni_5Fe_4$-0.40 % Ti alloy after forging was found to be 0.003916 mg/(dm^2·day) after 72 hours. The corrosion behavior of $CuAl_{10}Ni_5Fe_4$ alloy is significantly influenced by its microstructural phases, specifically the α, β, and κ phases. Understanding the roles of these phases is crucial for enhancing the alloy's corrosion resistance, particularly in aggressive environments such as saline solutions. The α phase, which is the primary phase in the $CuAl_{10}Ni_5Fe_4$ alloy, generally exhibits good corrosion resistance due to its stable microstructure.

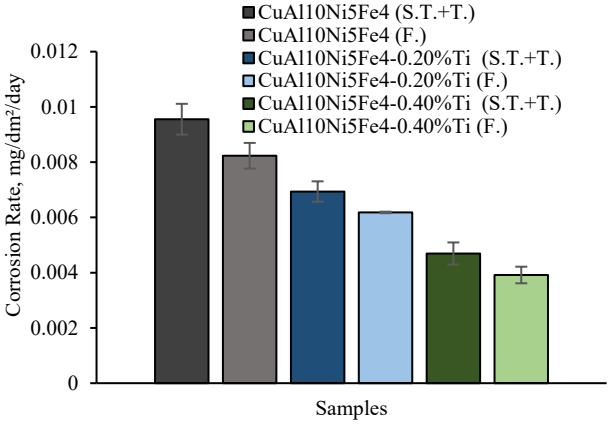

Fig. 9. Comparative immersion corrosion rates result of $CuAl_{10}Ni_5Fe_4$, $CuAl_{10}Ni_5Fe_4$-0.20 % Ti and $CuAl_{10}Ni_5Fe_4$-0.40 % Ti alloys. S.T. – solution treatment; T. – tempering; F. – forging

However, the presence of the β phase can lead to localized corrosion phenomena. The β phase, being more electrochemically active, can act as a galvanic cathode, promoting microgalvanic corrosion when it is discontinuously distributed within the matrix. This behavior is similar to findings in other alloys, where the β phase's volume fraction and distribution significantly affect corrosion rates and mechanisms [52, 53]. The κ phase, on the other hand, has been reported to enhance the mechanical properties of the $CuAl_{10}Ni_5Fe_4$ alloy without compromising its ductility. This phase contributes to the overall strength of the alloy, which can indirectly influence its corrosion resistance by improving the integrity of the microstructure under corrosive conditions [17, 32]. The presence of the κ phase can also help in reducing the susceptibility to stress corrosion cracking, as it may inhibit the formation of microcracks that can serve as initiation sites for corrosion. Moreover, the interaction between these phases can lead to complex corrosion behaviors. For instance, the presence of the β phase can lead to preferential anodic dissolution, while the κ phase can mitigate this effect by providing a more uniform microstructure that resists localized attack.

The corrosion resistance of nickel-aluminum bronze alloys can be improved by several processing techniques and alloying elements. The hot shaping of CuAl10Ni5Fe4 alloy enhances corrosion resistance by spheroidising and dispersing κ phases, hence diminishing selective phase corrosion [17].

The presence of specific phases in alloys can significantly influence their corrosion behavior. Furthermore, the corrosion potential of different phases within an alloy can vary, influencing the overall corrosion resistance [54]. In the context of bronze alloys, chloride ions have been identified to cause preferential corrosion of the

Cu-rich phase, while the α + β eutectic phase is susceptible to corrosion under specific oxygen conditions [55]. Furthermore, in nickel aluminum bronze, the microstructure has been found to influence crevice corrosion initiation, with specific phases such as the κ_{III} phase playing a role in corrosion within the microstructure [21]. The presence of CuO phase plays a significant role in the corrosion behavior of copper-based materials. Studies have shown that CuO is a predominant constituent in the corrosion product film formed on copper alloys after exposure to corrosive environments [56 – 58]. The formation of CuO has been linked to enhanced corrosion resistance due to its ability to reduce the number of corrosion sites and slow down the corrosion rate [59]. Additionally, CuO has been reported to be a stable species in neutral solutions, contributing to the formation of corrosion products like Cu_2O, which further influences the corrosion process [58]. Copper oxide (Cu_2O) is involved in the corrosion process of copper-based materials. Platzman et al. proposed a three-stage oxidation mechanism where a Cu_2O layer forms and then transforms into a more stable CuO layer [60]. The initial formation of Cu_2O is significant as it acts as a reservoir of Cu+ ions, triggering catalytic corrosion cycles [61]. Cu_2O has been observed to agglomerate into CuO particles during oxidation processes [62]. The presence of Cu_2O on copper materials influences their corrosion behavior, with corrosion products often being composed of Cu_2O [63 – 65]. The formation of Cu_2O can initiate corrosion cells, with the Cu_2O film acting as the cathode, contributing to pitting corrosion [66]. Cu_2O demonstrates high corrosion resistance and stability in various environments, enhancing protective properties [67]. In copper-nickel alloys, the incorporation of nickel ions in the Cu_2O barrier layer enhances corrosion resistance by reducing ionic conductivity within Cu_2O [68]. Cu_2O has also been linked to the corrosion resistance of copper under different conditions, such as in the presence of organic acids [69]. The protective role of Cu_2O patina in increasing corrosion resistance contrasts with the detrimental effects of $CuCl_2$ patina [69]. The corrosion resistance of copper alloys can vary significantly depending on the presence of different phases and elements within the alloy matrix. Additionally, the presence of specific phases such as Cu_2O and Cu-Al intermetallic phases can play a crucial role in either enhancing or reducing the corrosion resistance of copper alloys [70, 71]. Moreover, copper alloying elements, including the presence of grain boundaries and precipitates, can significantly impact the microstructure and corrosion behavior of the material. For example, the scarcity of alloying elements such as copper can keads to the formation of grain boundary segregation and increase the susceptibility of the alloy to intergranular corrosion [72, 73]. On the other hand, the presence of certain copper-rich precipitate phases, such as the τ-phase, can enhance the corrosion resistance by forming protective layers that inhibit corrosion processes [73]. Rahman et al. discussed the specific appearances of corrosion such as intercrystalline corrosion and corrosion cracking in copper alloys, emphasizing the effect of alloying elements on corrosion behaviour [74]. The presence of TiO phase in copper alloys has been shown to have a significant impact on their corrosion resistance. demonstrated that the addition of a TiO layer improved the corrosion resistance of Ti-containing alloys compared to those without Ti when exposed to elevated temperatures in molten salt environments [75]. The phase of TiO_2 plays a crucial role in influencing the corrosion behavior of copper alloys. Studies have shown that the corrosion rate of copper alloys can be affected by the presence of TiO_2. For instance, research by Saber et al. highlighted that Cu/Al_2O_3 composites exhibited lower corrosion rates compared to pure copper and copper coated with TiO_2 [76]. Moreover, the composition of copper alloys, including the presence of alloying elements, can also influence their corrosion resistance. This suggests that TiO plays a crucial role in enhancing the corrosion resistance of copper alloys under specific conditions. The presence of the Ti_3O_5 phase in copper alloys can significantly impact their corrosion behavior. Studies have shown that the formation of intermetallic compounds like Ti_2Cu can create an "envelope effect," which acts as a barrier preventing corrosive liquids from directly contacting the alloy, thereby enhancing its corrosion resistance [77]. Additionally, the equilibrium between Ti and O in alloys can lead to the solubility of other elements like Fe, Cr, and Ni in the Ti_3O_5 phase, affecting the overall corrosion properties of the material [78]. The presence of the Ti_2O phase in copper alloys has a significant impact on their corrosion behavior. Studies have shown that heat treatment can lead to the redistribution of copper elements and the precipitation of the Ti_2Cu phase, resulting in improved mechanical properties and corrosion resistance properties [77]. In the XRD analyses given in Fig. 10, while Cu_2O rich in copper is commonly found in the highest peak (42.60°); TiO, Ti_2O_3 and Ti_3O_5 phases are observed in this peak with titanium addition. The terminating peaks of the alloys are at 86.60° and Cu_2O and CuO phases are observed in the alloy without titanium addition; Ti_2O, Ti_2O_3 and Ti_3O_5 phases are observed in this peak with titanium additions. When the peaks of the $CuAl_{10}Ni_5Fe_4$ alloy are examined in Fig. 10 a, it starts with $CuCl_2$ at 18.45° and then the Cu_2O phase appears at 29.30°. In Fig. 10 b, $CuAl_{10}Ni_5Fe_4$-0.20 % Ti alloy started with $CuCl_2$ phase at 15.50° and immediately afterwards Ti_3O_5 phase was observed at 20.55°. In Fig. 10 c, in $CuAl_{10}Ni_5Fe_4$-0.40 % Ti alloy, $CuCl_2$ and Ti_3O_5 phases were observed at 16.60° while $CuCl_2$ and Ti_2O phases appeared at 21.70°.

Fig. 11 shows the SEM images of $CuAl_{10}Ni_5Fe_4$, $CuAl_{10}Ni_5Fe_4$-0.20 % Ti and $CuAl_{10}Ni_5Fe_4$-0.40 % Ti alloys corroded after solution treatment and tempering after casting, while Fig. 12 shows the SEM images of these alloys corroded after forging. Table 4 and Table 5 show the EDX analysis of the second phase with distinct morphologies labeled as (1-6) in Fig. 11 and Fig. 12, respectively. When the general SEM images are examined, it is seen that there are crater formations by layering in places. The frequency of pitted/porous structures and crater formations is remarkable in the images. A decrease in the frequency of these structures was observed in all alloys after forging. It is thought that $CuCl_2$ phase is formed in the areas where pitting corrosion occurs. In $CuAl_{10}Ni_5Fe_4$ (Fig. 11 a) alloy, which has been corroded after solution treatment and tempering after casting, branching-like pittings are observed in the pit at point 1. In EDX analyses, the highest Cl ion is observed in this region and therefore, it is possible to say that although $CuCl_2$ phase is dense at this point, a protective barrier for

corrosion is formed with the formation of CuO phase in the region. The crater formations at point 2 are thought to be Cu_2O corrosion phase. In $CuAl_{10}Ni_5Fe_4$-0.20 % Ti (Fig. 11 b) alloy, which has been corroded after solution treatment and tempering after casting, small pits are found in a sediment-like formation at point 3. Here, Ti_2O_3 and Ti_2O phases are thought to have formed, while TiO phase is assumed to have formed at point 4.

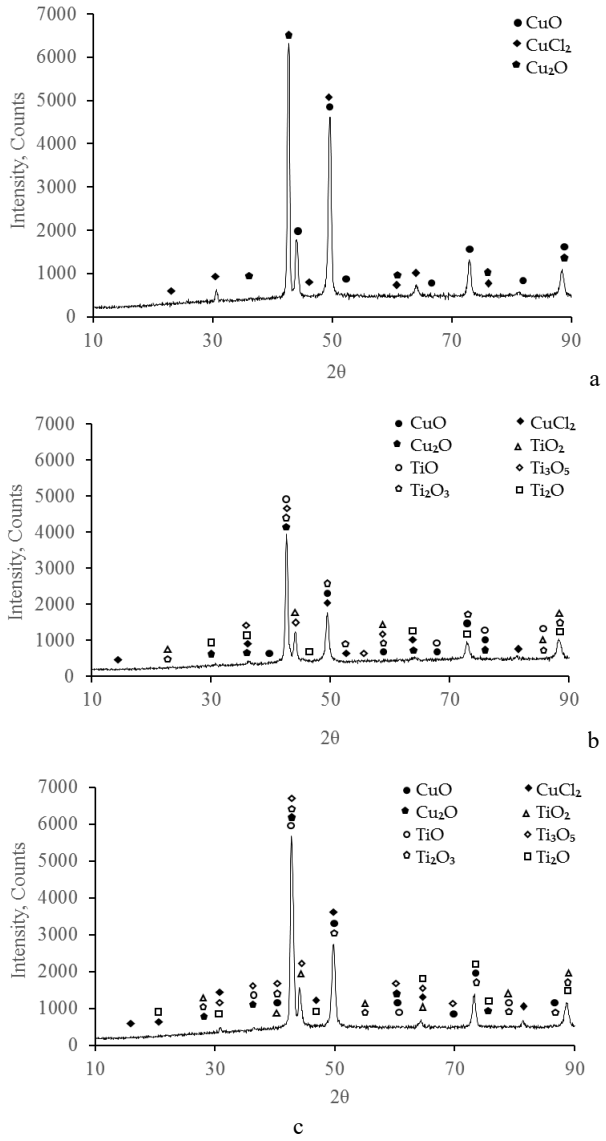

Fig. 10. X-ray diffraction patterns after corrosion: a – $CuAl_{10}Ni_5Fe_4$; b – $CuAl_{10}Ni_5Fe_4$-0.20 % Ti; c – $CuAl_{10}Ni_5Fe_4$-0.40 % Ti

Here, Ti_2O_3 and Ti_2O phases are thought to have formed, while TiO phase is assumed to have formed at point 4. In $CuAl_{10}Ni_5Fe_4$-0.40 % Ti (Fig. 11 c) alloy, which has been corroded after solution treatment and tempering after casting, Ti_2O and TiO are formed at point 5, while the stratified crater formation at point 6 is likely to be Ti_3O_5 and Ti_2O_3. After forging, $CuAl_{10}Ni_5Fe_4$ (Fig. 12 a) alloy that has been corroded, at point 1, in the area where there are sometimes round and sometimes linear pitting on the surface, it is thought that $CuCl_2$ and Cu_2O phases are formed. At point 2, CuO and Cu_2O phases are likely to form. After forging, $CuAl_{10}Ni_5Fe_4$-0.20 % Ti (Fig. 12 b) alloy that has been corroded, it is thought that the cause of the precipitation at point 3 is the $CuCl_2$ phase and the reason for this precipitation being irregular is the formation of the TiO_2 phase here.

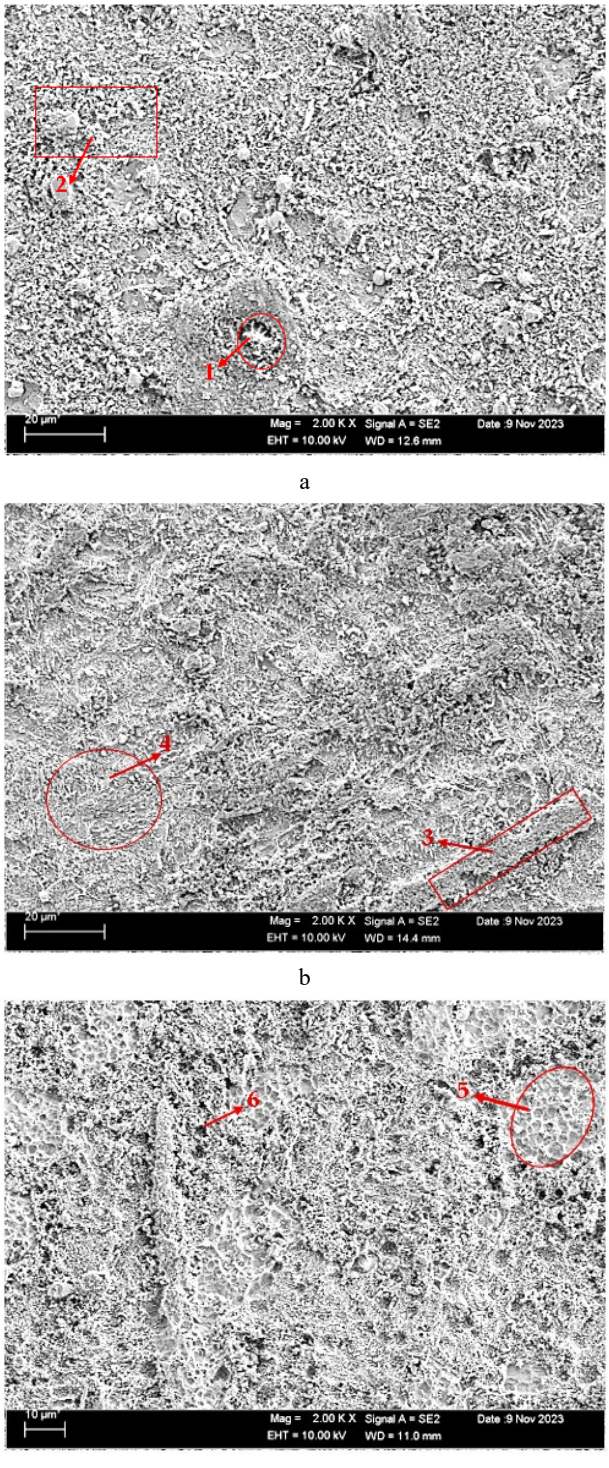

Fig. 11. SEM images of corrosion after solution treatment and tempering after casting: a – $CuAl_{10}Ni_5Fe_4$; b – $CuAl_{10}Ni_5Fe_4$-0.20 % Ti; c – $CuAl_{10}Ni_5Fe_4$-0.40 % Ti

The crater formation on the surface at point 4 is attributed to the TiO phase. After the forging process, it is thought that the TiO_2 phase is formed in contrast to the $CuCl_2$ phase in the pit-like structure that occurred at point 5 in the $CuAl_{10}Ni_5Fe_4$-0.40 % Ti (Fig. 12 c) alloy that has been corroded.

Table 4. The weight percentage findings of Fig. 11 as determined by EDX

Points	Al	Ti	Mn	Fe	Ni	Cu	Cl	O
1	10.65	–	0.86	15.20	5.76	1.56	15.14	50.77
2	12.83	–	1.58	25.44	19.85	28.26	2.36	9.71
3	6.61	6.91	0.48	15.16	11.05	44.18	1.32	14.32
4	11.29	0.39	1.31	11.73	11.74	59.41	0.60	3.55
5	10.07	0.23	0.72	8.78	11.73	64.34	0.33	3.83
6	10.87	7.24	0.37	11.60	11.12	41.96	0.55	16.32

Table 5. The weight percentage findings of Fig. 12 as determined by EDX

Points	Al	Ti	Mn	Fe	Ni	Cu	Cl	O
1	11.11	–	1.24	27.72	12.10	43.20	1.92	2.73
2	16.76	–	0.53	14.40	23.87	34.81	0.87	8.78
3	7.48	1.26	1.29	10.35	7.55	65.52	0.54	7.17
4	14.92	0.29	1.38	13.21	20.14	41.01	0.20	8.85
5	11.25	5.08	3.40	29.21	13.64	34.30	0.54	2.59
6	11.63	7.70	1.32	20.67	15.10	35.16	0.45	7.98

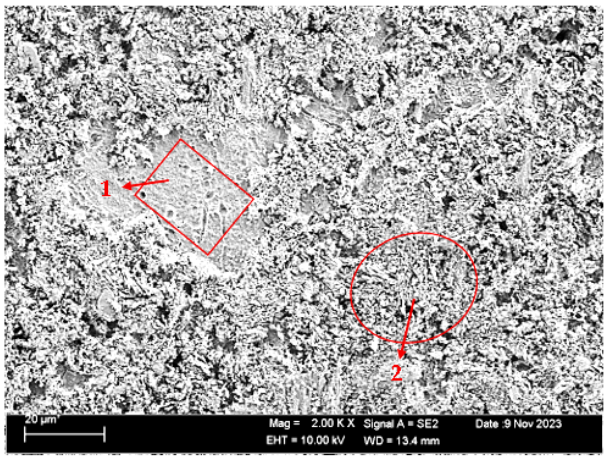

a

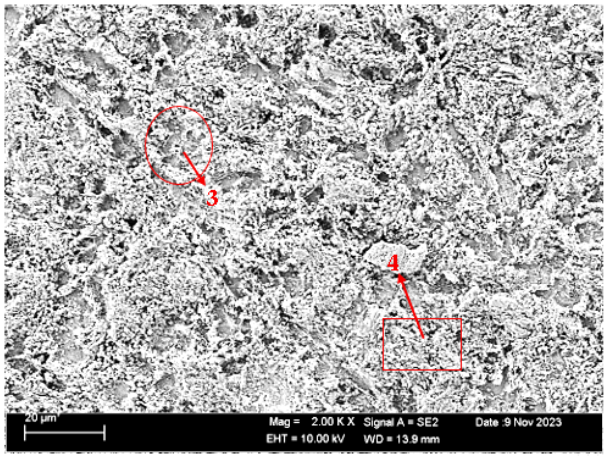

b

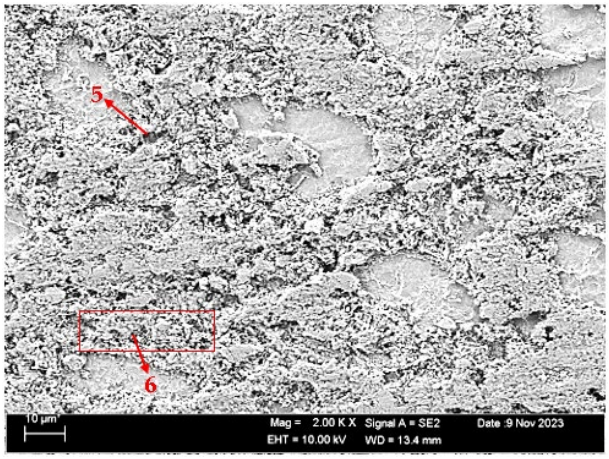

c

Fig. 12. SEM images of corrosion after forging: a – $CuAl_{10}Ni_5Fe_4$; b – $CuAl_{10}Ni_5Fe_4$-0.20 % Ti; c – $CuAl_{10}Ni_5Fe_4$-0.40 % Ti

At point 6, there is a regular crater formation and as can be seen from the EDX analysis, it is likely that this formation consists of Ti_3O_5 and Ti_2O_3 phases, which are titanium-rich phases. Investigations into copper corrosion in chloride-containing environments laden settings uncover intricate processes and the development of protective layers. In dilute oxychloride solutions, copper initially dissolves as CuCl2-, thereafter undergoing hydrolysis and oxide production on the surface [79].

Protective scales including CuO or Cu2O can rapidly develop, becoming progressively less porous over time [80]. On Cu-Ni-Fe alloys, a dual-layer protective film develops: a substantial outer layer predominantly composed of Cu_2O and a slender interior layer enriched with chloride, oxygen, and [81]. The maximum chloride concentration is frequently detected near the boundary between these layers. Although alkanethiol layers can safeguard copper against corrosion, their efficacy diminishes with increased chloride concentrations and at potentials conducive to the formation of Cu(II) oxide [81].

4. CONCLUSIONS

In this study, it was investigated how the corrosion and microstructural properties of 0.20 % and 0.40 % titanium added nickel aluminum bronze ($CuAl_{10}Ni_5Fe_4$) were affected by post-casting heat treatment (solution treatment and tempering) and forging methods. The results are as follows:

The microstructures of the heat-treated $CuAl_{10}Ni_5Fe_4$ alloy showed the presence of a copper-rich α-solid solution phase, a martensitic β-phase, and various intermetallic κ-phases including flake-shaped κI, fine κIII, and black globular κIV. It is shown that the addition of 0.20 % and

0.40 % titanium to $CuAl_{10}Ni_5Fe_4$ alloys resulted in a decrease in the dendritic arm thickness and an increase in the amount of certain types of κ phases. In the microstructures of $CuAl_{10}Ni_5Fe_4$, $CuAl_{10}Ni_5Fe_4$-0.20 % Ti, and $CuAl_{10}Ni_5Fe_4$-0.40 % Ti alloys, a significant decrease in grain size and a transformation of broken dendritic arms into almost spherical shapes were observed after forging.

The $CuAl_{10}Ni_5Fe_4$ alloy has lesser hardness than other alloys without titanium. Titanium reduces grain size and increases dislocation density, increasing hardness. The increase in stiff phases, such as tempered β and fine κIV, may also contribute to the increase in hardness. Forging and heat treatment increased the hardness of all three alloys, however $CuAl_{10}Ni_5Fe_4$-0.20 % Ti and $CuAl_{10}Ni_5Fe_4$-0.40 % Ti alloys had similar hardness values but were harder than $CuAl_{10}Ni_5Fe_4$.

After 24 hours, the forged $CuAl_{10}Ni_5Fe_4$-0.40 % Ti alloy experienced 0.003326 mg/dm² weight loss, while the $CuAl_{10}Ni_5Fe_4$ alloy experienced 0.013659 mg/dm² weight loss after solution treatment and tempering. The minimal corrosion rate in $CuAl_{10}Ni_5Fe_4$-0.40 % Ti alloy after forging was 0.003916 mg/(dm²·day) after 72 hours. Pitted/porous structures and craters are observed as corrosion damages. All alloys have less corrosive damages after forging. It is believed that the $CuCl_2$ phase forms in regions of pitting corrosion.

REFERENCES

1. **Ocejo, I., Biezma, M., Linhardt, P.** Corrosion Evaluation of Welded Nickel Aluminum Bronze and Manganese Aluminum Bronze in Synthetic Sea Water *Materials and Corrosion* 73 (11) 2022: pp. 1788 – 1799. https://doi.org/10.1002/maco.2022133282
2. **Wannaprawat, N., Karuna, T.** Study of Deep Cryogenic Treatment Process Effect on Microstructure and Properties of CuBeZr Alloy *Key Engineering Materials* 841 2020: pp. 335 – 339. https://doi.org/10.4028/www.scientific.net/KEM.841.335
3. **Oluwadare, B. S., Adebayo, A., Stephen, J.T.** The Influence of the Addition of Nickel on the Structure and Mechanical Properties of Aluminium Bronze Alloy *Review of Industrial Engineering Letters* 5 2019: pp. 12 – 21. https://doi.org/10.18488/journal.71/2019.51.12.21
4. **Figueiredo, E., Pereira, M.A.S., Lopes, F., Marques, J.G., Santos, J.P., Araújo, M.F., Silva, R.J.C., Senna-Martinez, J.C.** Investigating Early/Middle Bronze Age Copper and Bronze Axes by Micro X-Ray Fluorescence Spectrometry and Neutron Imaging Techniques *Spectrochimica Acta Part B: Atomic Spectroscopy* 122 2016: pp. 15 – 22. https://doi.org/10.1016/j.sab.2016.05.002
5. **Avila de Melo, A., Cardoso, J., Giumlia-Mair, A.** Tapada Da Ajuda (Lisbon, Portugal) Bronze Age Pin *Materials and Manufacturing Processes* 32 2016: pp. 792 – 797. https://doi.org/10.1080/10426914.2016.1232824
6. **Oudbashi, O., Emami, M., Davami, P.** Bronze in Archaeology: A Review of the Archaeometallurgy of Bronze in Ancient Iran. In; 2012.
7. **Oudbashi, O., Naseri, R., Malekzadeh, M.** Technical Studies on the Bronze Age Metal Artefacts from the Graveyard of Deh Dumen, South-Western Iran (Third Millennium BC) *Archaeometry* 58 2016: pp. 947 – 965 https://doi.org/10.1111/arcm.12208
8. **Oudbashi, O., Hassanpour, A.** Microscopic Study on Some Iron Age Bronze Objects from Western Iran *Heritage Science* 4 2016: pp. 1 – 8. https://doi.org/10.1186/s40494-016-0079-0
9. **Figueiredo, E., Silva, R.J.C., Senna-Martinez, J.C., Araújo, M.F., Braz Fernandes, F.M., Inês Vaz, J.L.** Smelting and Recycling Evidences from the Late Bronze Age Habitat Site of Baiões (Viseu, Portugal) *Journal of Archaeological Science* 37 2010: pp. 1623 – 1634. https://doi.org/10.1016/j.jas.2010.01.023
10. **Valério, P., Monge Soares, A.M., Fátima Araújo, M., Silva, R.J.C., Porfírio, E., Serra, M.** Arsenical Copper and Bronze in Middle Bronze Age Burial Sites of Southern Portugal: The First Bronzes in Southwestern Iberia *Journal of Archaeological Science* 42 2014: pp. 68 – 80. https://doi.org/10.1016/j.jas.2013.10.039
11. **El-Mahallawy, N., Majed, A., Maboud, A.A.G.A.** Effect of FSP Process Parameters with Air Blowing on Microstructure and Hardness of NiAl Bronze Alloy *Materials Research Express* 7 2020: pp. 016590. https://doi.org/10.1088/2053-1591/ab691a
12. **Lv, Y., Ding, Y., Han, Y., Zhang, L.C., Wang, L., Lu, W.** Strengthening Mechanism of Friction Stir Processed and Post Heat Treated NiAl Bronze Alloy: Effect of Rotation Rates *Materials Science and Engineering: A* 685 2017: pp. 439 – 446. https://doi.org/10.1016/j.msea.2016.12.050
13. **Venkatesan, S., Jerald, J., Sundeep, D., Vardharaj, E. K., Sastry, C. C.** Evaluation of Mechanical and Corrosion Properties of TiB_2-Y_2O_3 Nanocomposite Fused Bronze Metal Matrix Composite *Surface Topography: Metrology and Properties* 10 2022: pp. 1 – 17. https://doi.org/10.1088/2051-672X/ac7faa
14. **Biezma, M., Rasilla, O., Haubner, R., Linhardt, P.** Etching of Manganese Aluminum Bronze by Ultrasound in Seawater *Practical Metallography* 59 2022: pp. 236 – 250. https://doi.org/10.1515/pm-2022-0027
15. **Wu, Z., Hu, Q., Qin, Z., Zhang, Y., Xia, D.H., Hu, W.** Effect of Plastic Deformation on Mechanical Properties and Corrosion Resistance of Nickel-Aluminum Bronze *Anti-Corrosion Methods and Materials* 68 2021: pp. 473 – 480. https://doi.org/10.1108/ACMM-12-2020-2411
16. **Qin, Z., Zhang, Q., Luo, Q., Wu, Z., Shen, B., Lei, L., Hu, W.** Microstructure Design to Improve the Corrosion and Cavitation Corrosion Resistance of a Nickel-Aluminum Bronze *Corrosion Science* 139 2018: pp. 255 – 266. https://doi.org/10.1016/j.corsci.2018.04.043
17. **Kulakli, A., Şeşen, F., Çitrak, T., Özeren, T.** Effect of Cobalt and Titanium Additions on Corrosion and Wear Resistance of Nickel Containing Aluminum Bronzes *Metal 2020* 2020: pp. 1135 – 1141.
18. **Anene, F., Nwankwo, N., Nwoke, V.** Effect of Dopant and Heat Treatment on the Microstructure and Mechanical Properties of Nickel-Aluminum Bronze *Metallurgical and Materials Engineering* 25 2019: pp. 147 – 162. https://doi.org/10.30544/423
19. **Zhang, B.B., Wang, J.Z., Yuan, J.Y., Yan, F.Y.** Tribocorrosion Behavior of Nickel Aluminum Bronze in Seawater: Identification of Corrosion-wear Components and Effect of pH *Materials and Corrosion* 69 2017: pp. 106 – 114. https://doi.org/10.1002/maco.201709648
20. **Vakilipour Takaloo, A.** Corrosion Behavior of Heat Treated Nickel-Aluminum Bronze Alloy in Artificial Seawater

Materials Sciences and Applications 02 2011: pp. 1542 – 1555. https://doi.org/10.4236/msa.2011.211207

21. **Wharton, J., Stokes, K.** The Influence of Nickel–Aluminium Bronze Microstructure and Crevice Solution on the Initiation of Crevice Corrosion *Electrochimica Acta* 53 2008: pp. 2463 – 2473. https://doi.org/10.1016/j.electacta.2007.10.047
22. **Ding, Y., Zhao, R., Qin, Z., Wu, Z., Wang, L., Lei, L., Lu, W.** Evolution of the Corrosion Product Film on Nickel-Aluminum Bronze and Its Corrosion Behavior in 3.5 wt.% NaCl Solution *Materials* 12 2019: pp. 209. https://doi.org/10.3390/ma12020209
23. **Wu, Z., Cheng, Y., Lei, L., Lv, W., Hu, W.** Effect of Heat Treatment on Microstructure Evolution and Erosion-Corrosion Behavior of a Nickel-Aluminum Bronze Alloy in Chloride Solution *Corrosion Science* 98 2015: pp. 260 – 270. https://doi.org/10.1016/j.corsci.2015.05.037
24. **Hasan, F., Jahanafrooz, A., Lorimer, G.W., Ridley, N.** The Morphology, Crystallography, and Chemistry of Phases in as-Cast Nickel-Aluminum Bronze *Metallurgical Transactions A* 13 1982: pp. 1337 – 1345. https://doi.org/10.1007/BF02642870
25. **Babalola, B., Bodunrin, M., Borode, J.O., Alaneme, K.** Corrosion Characteristics of As-Cast Aluminium Bronze Alloy in Selected Aggressive Media *Journal of Minerals and Materials Characterization and Engineering* 01 2013: pp. 245 – 249. https://doi.org/10.4236/jmmce.2013.15038
26. **Meigh, H.** *Cast and Wrought Aluminium Bronzes: Properties, Processes and Structure,* 2018.
27. **Hasan, F., Lorimer, G., Ridley, N.** Tempering of Cast Nickel–Aluminium Bronze *Metal Science* 17 1983: pp. 289 – 296. https://doi.org/10.1179/030634583790420826
28. **Chen, R., Liang, Z., Zhang, W., Zhang, D., Luo, Z., Li, Y.** Effect of Heat Treatment on Microstructure and Properties of Hot-Extruded Nickel-Aluminum Bronze *Transactions of Nonferrous Metals Society of China* 17 2007: pp. 1254 – 1258. https://doi.org/10.1016/S1003-6326(07)60258-1
29. **Anantapong, J., Uthaisangsuk, V., Suranuntchai, S., Manonukul, A.** Effect of Hot Working on Microstructure Evolution of As-Cast Nickel Aluminum Bronze Alloy *Materials & Design* 60 2014: pp. 233 – 243. https://doi.org/10.1016/j.matdes.2014.03.033
30. **Mund, K., Richter, G., Sturm, F.** Titanium-Containing Raney Nickel Catalyst for Hydrogen Electrodes in Alkaline Fuel Cell Systems *Journal of The Electrochemical Society* 124 1977: pp. 1 – 6. https://doi.org/10.1149/1.2133234
31. **Lv, Y., Wang, L., Han, Y., Xu, X., Lu, W.** Investigation of Microstructure and Mechanical Properties of Hot Worked NiAl Bronze Alloy with Different Deformation Degree *Materials Science and Engineering: A* 643 2015: 17 – 24. https://doi.org/10.1016/j.msea.2015.06.078
32. **Öztürk, S., Sünbül, S., Metoğlu, A., Önal, S., İcin, K.** Characterisation of Nickel–Aluminium Bronze Powders Produced by the Planar Flow Casting Method *Materials Science and Technology* 36 2020: pp. 1771 – 1784. https://doi.org/10.1080/02670836.2020.1834681
33. **Daroonparvar, M., Atabaki, M., Vakilipour, A.** Effect of Pre-Heat Treatment on Corrosion Behaviour of Nickel-Aluminum Bronze Alloy *Association of Metallurgical Engineers of Serbia* 17 (4) 2011: pp. 183 – 198.
34. **Yaseen, M., Mansoor, M., Ansari, H., Hussain, S., Khan, S.** Effect of Heat Treatment on Tribological Characteristics of CuAl10Ni5Fe4 Nickel Aluminum Bronze *Key Engineering Materials* 778 2018: pp. 61 – 67. https://doi.org/10.4028/www.scientific.net/KEM.778.61
35. **Ding, Y., Lv, Y., Chen, K., Zhao, B., Han, Y., Wang, L., Lu, W.** Effects of Microstructure on the Stress Corrosion Cracking Behavior of Nickel-Aluminum Bronze Alloy in 3.5% NaCl Solution *Materials Science and Engineering: A* 733 2018: pp. 361 – 373. https://doi.org/10.1016/j.msea.2018.07.066
36. **Hårsta, A., Rundqvist, S.** The Crystal Chemistry of Kappa-Phases *Journal of Solid State Chemistry* 70 1987: pp. 210 – 218. https://doi.org/10.1016/0022-4596(87)90058-2
37. **Recarte, V., Pérez-Landazabal, J.I., Campo, J., Pérez-Saez, R.B., No, M.L., Juan, J.S.** In Situ Study of the β Phase Decomposition Process in a Cu-Al-Ni Shape Memory Alloy Processed by Powder Metallurgy *Journal de Physique IV France* 112 2003: pp. 605 – 609. https://doi.org/10.1051/jp4:2003958
38. **Pérez-Landazábal, J.I., Recarte, V., Sánchez-Alarcos, V.** Influence on the Martensitic Transformation of the β Phase Decomposition Process in a Cu-Al-Ni Shape Memory Alloy *Journal of Physics: Condensed Matte* 17 2005: pp. 4223. https://doi.org/10.1088/0953-8984/17/26/019
39. **Rodriguez, P., Guenin, G.** Thermal Aging Behaviour and Origin of a Cu Al Ni Shape Memory Alloy *Materials Science and Engineering: A* 129 1990: pp. 273 – 277. https://doi.org/10.1016/0921-5093(90)90274-7
40. **Thossatheppitak, B., Suranuntchai, S., Uthaisangsuk, V., Manonukul, A., Mungsantisuk, P.** Microstructure Evolution of Nickel Aluminum Bronze Alloy during Compression at Elevated Temperatures *Advanced Materials Research* 893 2014: pp. 365 – 370. https://doi.org/10.4028/www.scientific.net/AMR.893.365
41. **Nabach, W. A** The Effects of Isothermal Deformation and Annealing on the Microstructure of Nickel-Aluminum-Bronze Propeller Material. Naval Postgraduate School, Monterey, California, 2003: pp. 7 – 14.
42. **Barik, R. C., Wharton, J. A., Wood, R. J. K., Stokes, K. R.** Nickel-Aluminium Bronze Pitting Corrosion in Seawater Environment and Mitigation *In Proceedings of the EUROCORR Conference*, 6–10 September, 2009.
43. **Parameswaran, P., Rameshbabu, A.M., Gopal, N., Yogeshwaran, R., Ramkumar, R.** Study of the Corrosion Properties in a Hot Forged Cu-Al-Ni Alloy with Added Cr *Journal of the Mechanical Behavior of Materials* 27 2018: pp. 1 – 6. https://doi.org/10.1515/jmbm-2018-0016
44. **Carsi, M., Penalba, F., Rieiro, I., Zapirdin, F., Ruano, O.** Hot Forging of a Cu-Al-Ni-Fe-Mn Alloy and Its Simulation by Torsion Testing *International Journal of Materials Research* 91 (12) 2000: pp. 1057 – 1062. https://doi.org/10.1515/ijmr-2000-911216
45. **Long, B.T., Kim, Y.H., Ishizaki, K., Toan, N.D., Parinov, I.A., Vu, N.P., Eds.;** Lecture Notes in Mechanical Engineering; Springer International Publishing: Cham, 2021 *Proceedings of the 2nd Annual International Conference on Material, Machines and Methods for Sustainable Development (MMMS2020)*.
46. **Adamiak, M., Appiah, A., Woźniak, A., Nuckowski, P., Nazarov, S., Ganiev, I.** Impact of Titanium Addition on

Microstructure, Corrosion Resistance, and Hardness of As-Cast Al+6%Li Alloy *Materials* 16 2023: pp. 2671. https://doi.org/10.3390/ma16072671

47. **Lan, L., Xin, R., Jin, X., Gao, S., He, B., Rong, Y., Min, N.** Effects of Laser Shock Peening on Microstructure and Properties of Ti-6Al-4V Titanium Alloy Fabricated via Selective Laser Melting *Materials* 13 2020: pp. 3261. https://doi.org/10.3390/ma13153261
48. **Huang, Y., Liu, H., Xiao, Z., Sanxing, W.** Poisoning of Zr Microstructures during Casting Homogenisation and Solution Treatment *Materials Science and Technology* 34 2017: pp. 1 – 7. https://doi.org/10.1080/02670836.2017.1353661
49. **Souza E Silva, C.C., Santos, V.T., Lobo, F.G., Silva, M.R., Santos, G.A., Vasconcellos, S.P., Silva, R.A.G.** Phase Stability and Unidirectional Solidification in a Ni-Al Bronze *Journal of Materials Research and Technology* 25 2023: pp. 2240 – 2250. https://doi.org/10.1016/j.jmrt.2023.06.030
50. **Nascimento, M., Santos, G., Teram, R., Torres dos Santos, V., Silva, M., Couto, A.** Effects of Thermal Variables of Solidification on the Microstructure, Hardness, and Microhardness of Cu-Al-Ni-Fe Alloys *Materials* 12 2019: pp. 1267. https://doi.org/10.3390/ma12081267
51. **Aydogdu, A., Aydogdu, Y., Adigüzel, O.** Improvement of Hardness and Microstructures by Ageing in ShapeMemory CuAlNi Alloys *Journal de Physique IV France* 07 1997: pp. C5-311 – C5-316. https://doi.org/10.1051/jp4:1997549
52. **Zhang, J., Wang, Z., Cai, H., Ming, Z., Niu, L.** Corrosion Behavior of AZ91/AZ91-0.4%Nd Alloys in 3.5wt.% NaCl *Applied Mechanics and Materials* 291 – 294 2013: pp. 699 – 702. https://doi.org/10.4028/www.scientific.net/AMM.291-294.699
53. **Song, Y., Wang, Z., Liu, Y., Yang, M., Qu, Q.** Influence of Erbium, Cerium on the Stress Corrosion Cracking Behavior of AZ91 Alloy in Humid Atmosphere: Influence of Erbium, Cerium on the Stress Corrosion Cracking Behavior *Advanced Engineering Materials* 19 2017: pp. 1700021. https://doi.org/10.1002/adem.201700021
54. **Zhang, J., Wang, Z., Sun, W., Ming, Z.** Microstructure and Corrosion Behavior of AZ91-0.4%Nd Magnesium Alloy *Applied Mechanics and Materials* 291 2013: pp. 2577 – 2580. https://doi.org/10.4028/www.scientific.net/AMM.291-294.2577
55. **Song, Z., Tegus, O.** The Corrosion Properties of Bronze Alloys in NaCl Solutions *Materials* 16 2023: pp. 5144. https://doi.org/10.3390/ma16145144
56. **Jin, T., Zhang, W., Li, N., Liu, X., Han, L., Dai, W.** Surface Characterization and Corrosion Behavior of 90/10 Copper-Nickel Alloy in Marine Environment *Materials* 12 2019: pp. 1869. https://doi.org/10.3390/ma12111869
57. **Chen, Z., Persson, D., Samie, F., Zakipour, S., Leygraf, C.** Effect of Carbon Dioxide on Sodium Chloride-Induced Atmospheric Corrosion of Copper *Journal of The Electrochemical Society* 152 2005: pp. B502 – B511. https://doi.org/10.1149/1.2098327
58. **Lu, L., Li, X.** Corrosion Products of Reverse Crevice Corrosion of Copper *International Journal of Minerals, Metallurgy, and Materials* 18 2011: pp. 320 – 324. https://doi.org/10.1007/s12613-011-0441-x
59. **AbdElrhiem, E., Mohamed, S. G., Barakat, Y. F., Mostafa, M. M., Nada, R. H., Abdelaziz, S. M.** Corrosion Behavior and Microstructure of Al–10Zn Alloy with Nano CuO Addition *Scientific Reports* 13 2023: pp. 12855. https://doi.org/10.1038/s41598-023-39515-6
60. **Gattinoni, C., Michaelides, A.** Atomistic Details of Oxide Surfaces and Surface Oxidation: The Example of Copper and its Oxides *Surface Science Reports* 70 2015: pp. 424 – 447. https://doi.org/10.1016/j.surfrep.2015.07.001
61. **Li, X., Filice, F. P, Henderson, J. D, Behazin, M., Ramamurthy, S., Barker, I., Moshrefi, R., Skaanvik, S. A., Gateman, S. M., Shoesmith, D. W., Noël, J. J.** Particle-Particle Interface Corrosion of Cold Sprayed Copper in Dilute Nitric Acid Solution: Geometry-Controlled Corrosion Mechanism *Materials Degradation* 9 (1) 2025: pp. 1 – 10. https://doi.org/10.1038/s41529-025-00562-1
62. **Su, J., Jiang, M., Wang, H., Liu, Y.** Microstructure-Dependent Oxidation-Assisted Dealloying of Cu0.7Al0.3 Thin Films *Russian Journal of Electrochemistry* 51 2015: pp. 827 – 832. https://doi.org/10.1134/S102319351509013X
63. **Zhu, Y., Wang, J., Liu, H., Ren, P., Yan, F.** Effect of Dissolved Oxygen Content on Tribo-Corrosion Behavior of Monel 400 Alloy in Seawater *Metals* 14 2023: pp. 6. https://doi.org/10.3390/met14010006
64. **Shao, G., Gao, Y., Wu, J., Liu, P., Zhang, K., Li, W., Ma, F., Zhou, H., Chen, X.** Effect of Fe/Mn Content on Mechanical and Corrosion Properties of 90/10 Copper-Nickel Alloy *Materials and Corrosion* 73 2022: pp. 1085 – 1098. https://doi.org/10.1002/maco.202112748
65. **Li, G., Wenlong, C., Qiuling, H., Sichong, J., Peng, Z., Lianhua, L.** An Investigation into the Factors and Mechanisms Underlying Corrosion Failure of B10 Copper Tubes in Shipboard Pipelines *Journal of Physics: Conference Series* 2639 2023: pp. 012049. https://doi.org/10.1088/1742-6596/2639/1/012049
66. **Xie, J., Teng, Y., Zhang, L., Li, H.** Analysis and Prevention of Copper Pipe Corrosion *Journal of Physics: Conference Series* 2720 2024: pp. 012035. https://doi.org/10.1088/1742-6596/2720/1/012035
67. **Alshammari, K., Alhassan, S., Alshammari, A., Alotaibi, T., Alshammari, M., Hemaida, T., Alotibi, S., Henini, M.** Direct Synthesis of Sodium Doped Cu_2O/GO Nanocomposites for Catalytic Hydrogen Production from NaBH4 *Diamond and Related Materials* 137 2023: pp. 110148. https://doi.org/10.1016/j.diamond.2023.110148
68. **Biezma, M., Linhardt, P., Strobl, S., Haubner, R.** Influence of Annealing Treatments on Welded CuNi Sheets on the Corrosion Behaviour in Sea Water *BHM Berg- und Hüttenmännische Monatshefte* 166 2021: pp. 1 – 9. https://doi.org/10.1007/s00501-021-01131-0
69. **Chen, C., Cai, L., Wang, X., Wang, Y., Zhang, L., Zhou, H., Wu, L., Yan, Y.** Corrosion Behavior of Bronze under Organic Acid-Containing Thin Electrolyte Layer *Materials and Corrosion* 70 2018: pp. 319 – 327. https://doi.org/10.1002/maco.201810413
70. **Ding, K., Fan, L., Yu, M., Guo, W., Hou, J., Lin, C.** Sea Water Corrosion Behaviour of T2 and 12832 Copper Alloy Materials in Different Sea Areas *Corrosion Engineering, Science and Technology* 54 2019: pp. 1 – 9. https://doi.org/10.1080/1478422X.2019.1619289
71. **Rao, K., Kalvala, P.** Corrosion Resistance of AA2219 Aluminium Alloy: Electrochemical Polarisation and Impedance Study *Materials Science and Technology* 22 2006: pp. 97 – 104.

https://doi.org/10.1179/174328406X79405

72. **Braun, R.** Investigation on Microstructure and Corrosion Behaviour of 6XXX Series Aluminium Alloys *Materials Science Forum* 519 – 521 2006: pp. 735 – 740. https://doi.org/10.4028/www.scientific.net/MSF.519-521.735
73. **Unocic, K., Kobe, P., Mills, M., Daehn, G.** Grain Boundary Precipitate Modification for Improved Intergranular Corrosion Resistance *Materials Science Forum* 519 – 521 2006: pp. 327 – 332. https://doi.org/10.4028/www.scientific.net/MSF.519-521.327
74. **Rahman, M.M., Ahmed, S., Kaiser, M.** Corrosion Behavior of Work Hardened SnPb-Solder Affected Copper in the Bay of Bengal Water Environment *Advances in Materials Science and Engineering* 2022 2022: pp. 1 – 14. https://doi.org/10.1155/2022/2513391
75. **Kumar, M., Kant, R., Chand, S., Prakash, U., Sehgal, S., Saxena, K., Davim, J.P., Prakash, C.** High-Temperature Corrosion Performance of FeAl-Based Alloys Containing Carbon in Molten Salt *Metals* 11 2021: pp. 2040. https://doi.org/10.3390/met11122040
76. **Saber, D., Abdel-Aziz, K., Felemban, B., Alghtani, A., Ali, H., Ahmed, E., Megahed, M.** Characterization and Performance Evaluation of Cu-Based/TiO_2 Nano Composites. *Scientific Reports* 12 2022: pp. 1 – 14. https://doi.org/10.1038/s41598-022-10616-y
77. **Bao, M., Liu, Y., Wang, X., Yang, L., Li, S., Ren, J., Qin, G., Zhang, E.** Optimization of Mechanical Properties, Biocorrosion Properties and Antibacterial Properties of Wrought Ti-3Cu Alloy by Heat Treatment *Bioactive Materials* 3 2018: pp. 28 – 38. https://doi.org/10.1016/j.bioactmat.2018.01.004
78. **Seok, S.H., Miki, T., Hino, M.** Equilibrium between Ti and O in Molten Fe-Ni, Fe-Cr and Fe-Cr-Ni Alloys Equilibrated with 'Ti3O5' Solid Solution *ISIJ International* 51 2011: pp. 566 – 572. https://doi.org/10.2355/isijinternational.51.566
79. **Kim, G.Y., Jang, J., Woo, J.H., Yoon, S., Kim, J.S.** Electrochemical and Surface Investigations of Copper Corrosion in Dilute Oxychloride Solution *Nuclear Engineering and Technology* 55 2023: pp. 2742 – 2746. https://doi.org/10.1016/j.net.2023.05.021
80. **Zhe, Y., Pehkonen, S.O.** Copper Corrosion Kinetics and Mechanisms in the Presence of Chlorine and Orthophosphate *Water Science and Technology* 49 2004: pp. 73 – 81. https://doi.org/10.2166/wst.2004.0092
81. **Kato, C., Castle, J.E., Ateya, B.G., Pickering, H.W.** On the Mechanism of Corrosion of Cu-9.4Ni-l.7Fe Alloy in Air Saturated Aqueous NaCi Solution : II . Composition of the Protective Surface Layer. *Journal of The Electrochemical Society* 127 (9) 1980: pp. 1897 – 1903.